

Wave-induced sediment resuspension in the Finnish Archipelago, Baltic Sea: Integrating field measurements with large-scale numerical model simulations

Jan-Victor Björkqvist¹, Mari Savela^{2,3}, Heidi Pettersson⁴, Victor Alari⁵, and Alf Norkko³

¹Norwegian Meteorological Institute, Allégaten 70, 5007, Bergen, Norway

²City of Helsinki, Työpajankatu 8, 00580 Helsinki, Finland

³Tvärminne Zoological Station, Faculty of Biological and Environmental Sciences, University of Helsinki, J.A. Palméns väg 260, 10900 Hangö, Finland

⁴Finnish Meteorological Institute, P.O. Box 503, 00101, Helsinki, Finland

⁵Department of Marine Systems, Tallinn University of Technology, Akadeemia tee 15a, 12618 Tallinn, Estonia

Correspondence: Jan-Victor Björkqvist (janvb@met.no)

Abstract. Sediment resuspension, driven by wind-wave-induced shear stress, is a key process influencing coastal water quality, biogeochemical cycles, and the transport of pollutants and organisms. The critical shear stress, τ_{cr} , is a central parameter in sediment transport models, since resuspension can occur when wave-induced shear stress exceeds the critical value. In this study, we implemented a high-resolution (20 m) spectral wave model to simulate near-bottom orbital velocities across the complex archipelago of southwestern Finland. We then used laboratory measurements from in situ sediment samples to determine a model for the critical shear stress that accounts for physical properties using the median grain size and the dry bulk density, and the time-varying biological variation using chlorophyll *a*. Our proposed model, $\tau_{cr}(d_{50}, \rho_B, \text{ChlA}(t))$, explained 66% of the variation of the measured critical stress for our data collected from three different sediment types (Mud, Sand and Mixed sediments). The modelled mean critical shear stress differed between sediment classes were 0.49 N m⁻² for Mud, 1.56 N m⁻² for Sand, and 1.02 N m⁻² for Mixed sediments. The variability in the critical shear stress around the mean values driven by a non-constant biological contribution was approximately 30% for Mud and Sand, and approximately 50% for Mixed sediments. Finally, we used a class-level map of the sea floor and the in situ grain size data to translate the wave model orbital velocities to near-bottom shear stresses. Based on the numerical model data, the critical shear stresses from the newly proposed model, $\tau_{cr}(d_{50}, \rho_B, \text{ChlA}(t))$, were rarely exceeded based on only wave-induced motions in most of the model grid, but could, nonetheless, be exceeded to up around 10% of the times in smaller areas.

Copyright statement. TEXT

1 Introduction

Sediment resuspension is a key process in shallow coastal environments, influencing water quality, nutrient dynamics, and overall ecosystem health (Edge et al., 2015; Green and Coco, 2014). Resuspension can release contaminants and nutrients from
20 sediments, increase turbidity, and redistribute sediment particles, thereby affecting biogeochemical cycles, primary production, seabed morphology, and benthic habitats (Heiskanen, 1998; Green and Coco, 2014).

In coastal areas, resuspension dynamics are primarily driven by wind waves and currents, which exert shear stress τ (N m^{-2}) on the seabed. When shear stress on the seabed exceeds the critical threshold (τ_{cr}), it is possible for sediment particles to be lifted into the water column – a process known as resuspension (Shields, 1936; Soulsby and Whitehouse, 1997). In shallow
25 waters where currents are typically weak, wave-induced shear stress is the dominant driver of sediment resuspension (Pascolo et al., 2018).

Critical shear stress depends on sediment properties, including grain size, bulk density, water content, and chlorophyll *a* and organic matter content (Grabowski et al., 2011). Grain size is a fundamental determinant of erodibility, but in fine sediments, cohesive forces – driven by electrochemical and biological interactions – become increasingly important (Black et al., 2002;
30 Roberts et al., 1998). Biological factors further modify sediment stability: benthic fauna influence porosity and sediment structure through bioturbation and feeding activities (Mulsow et al., 1998; Michaud et al., 2006; Harris et al., 2015), while vegetation dampens hydrodynamic forces and stabilizes sediments via root systems (Koch et al., 2007; Madsen et al., 2001). Consequently, critical shear stress and resuspension potential vary across space and time (Joensuu et al., 2018, 2020). Although sediment transport models often estimate critical shear stress from median grain size (d_{50}) (Dade et al., 1992), natural sediments
35 exhibit substantial variability (Grabowski et al., 2011). Seasonal biofilm formation by microphytobenthos can increase τ_{cr} by up to fourfold (Le Hir et al., 2007; Decho, 2000). Despite this complexity, sediment transport models often estimate τ_{cr} solely from median grain size (Dade et al., 1992), ignoring biological and seasonal variability, although a recent modelling study by Zhang et al. (2025) incorporated seasonal values of τ_{cr} .

To improve predictions of sediment resuspension, we integrate empirical data (Joensuu et al., 2018, 2020) into our modelling
40 approach. Our objectives are: (i) to use high-resolution wave simulations to map spatial variability in near-bottom shear stress, (ii) to develop a spatial and temporal seabed model integrating in situ data to estimate critical shear stress, and (iii) to estimate sediment resuspension probabilities based on model outputs.

Our study area is located in the Hanko archipelago on the northern coast and entrance of the Gulf of Finland, the Baltic Sea (Fig. 1). This region provides an optimal setting for investigating sediment resuspension processes as it is characterized by a
45 mosaic of islands with a diverse range of coastal habitats that capture the spatial variability in seabed composition and in the physical and biological factors regulating sediment erodibility and resuspension dynamics.

The Baltic Sea is a semi-enclosed, brackish, and shallow sea, with a mean depth of 54 m and negligible tidal currents. In the study area, bottom currents are generally weak, ranging from a few centimetres per second to a maximum of 10 cm s^{-1} under typical conditions (Westerlund et al., 2018). However, current speed can exceed 10 cm s^{-1} occasionally in narrow channels
50 or during upwelling events (Westerlund et al., 2018; Miettunen, 2024). Consequently, sediment resuspension is predominantly

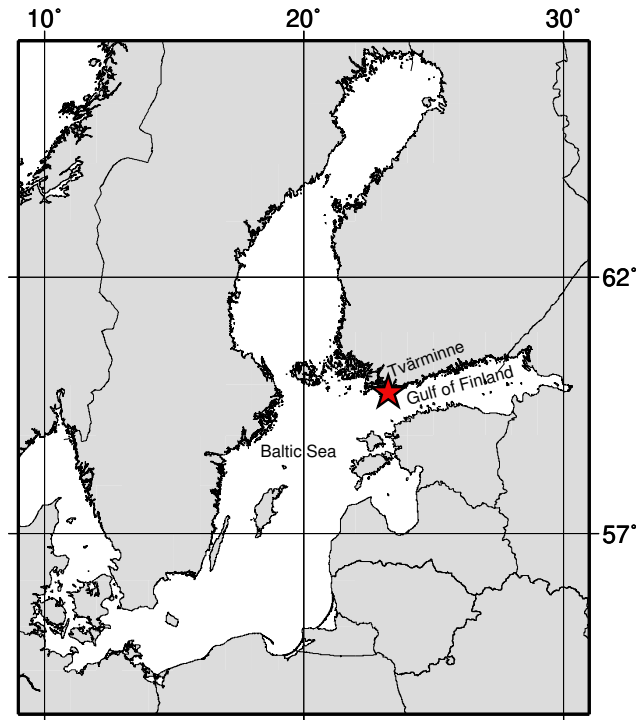


Figure 1. Location of the Tvärminne research station in the western Gulf of Finland, Baltic Sea.

governed by wind-wave induced shear stresses. Prevailing winds are from the southwest, with an average speed of $7\text{--}8\text{ m s}^{-1}$ (Alenius et al., 1998).

2 Wave data

2.1 Wave observations

55 Wave conditions were observed near Tvärminne research station in March and April 2017 using two Datawell Directional
 Waverider buoys: a larger 90 cm Mk-III at 24 m depth (outer archipelago) and a smaller 40 cm DWR-G4 at 17 m depth (inner
 archipelago) (Datawell, BV, 2025, 2024). Both buoys were located about 3 km east of the Tvärminne research station (Fig. 2).

Both wave buoys sampled at a frequency of 1.28 Hz and calculated the wave spectrum up to 0.58 Hz. Low-frequency data
 below 0.05 Hz were discarded when calculating wave parameters. These observations were used to validate the numerical wave
 60 model.

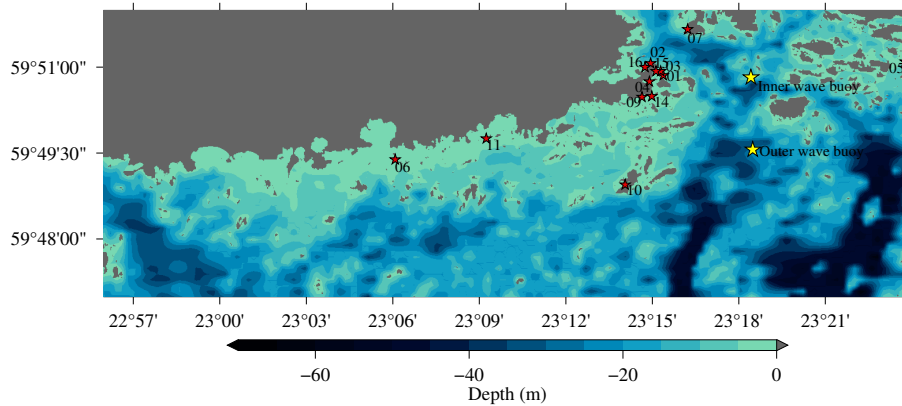


Figure 2. The bottom topography, in situ sediment sampling stations (01–16, marked by red stars), and wave buoy locations (yellow stars) are shown.

2.2 Wave simulations (SWAN)

The SWAN model (Booij et al., 1999) is a spectral wave model that was developed especially for shallow water and nearshore simulations. We implemented SWAN for 1 August – 30 September 2014 to catch the spatially extensive sediment measurement campaign (Joensuu et al., 2018), for 1 May – 30 November 2015 to cover the temporally extensive sediment measurement
65 campaign (Joensuu et al., 2020), and 1 March – 30 April 2017 to cover the period of the wave measurements (for validation purposes). Simulations were forced by data from a numerical FMI-HIRLAM weather prediction system (e.g. Eerola, 2013), where the wind speed and direction had been processed to a height of 10 meters. The wind data had a spatial resolution of roughly 7.4 km, and a 1 h temporal resolution for the years 2014 and 2015, and 3 h for 2017.

The model was implemented to a 0.01 nmi (~ 20 m) regular grid with lateral boundary conditions taken from a 1 nmi Baltic
70 Sea wide SWAN simulation using the same wind forcing. A 0.01 nmi resolution is higher than what is typically used in wave models, but SWAN has been implemented on a similar resolution before in the Baltic Sea (Alari and Raudsepp, 2012). Another spectral model has also been implemented on the North-American coast with an adaptive resolution up to 10 m (Abdolali et al., 2020). The available bathymetric data has been composed of data from nautical charts and the VELMU depth model (<https://ckan.ymparisto.fi/dataset/velmu-syvvyysmalli>) by the Finnish Environment Institute (SYKE) and had a resolution of 0.1
75 nmi. The land–sea mask has been rasterized based on a polygon dataset from SYKE (<https://ckan.ymparisto.fi/dataset/ranta10-rantaviiva-1-10-000>) and was available at a 0.01 nmi resolution. Land points were edited to wet points in the 0.1 nmi bathymetrical grid using the surrounding depth information. Additional depth information from Joensuu et al. (2018), Valanko (2012), and field sampling were used. The final 0.1 nmi grid was bi-linearly interpolated to a resolution of 0.01 nmi and the land-sea mask was applied (Fig. 2).

80 The wave model produced direct hourly gridded estimates of the maximum near-bottom orbital velocity, U_{bot} (m s^{-1}), and the near-bottom mean periods, $T_{m_{bot}}$ (s). The near-bottom amplitudes, a_{bot} (m), were determined directly by the velocity and period estimates. For a full definition of the wave parameters, see Appendix A.

During the simulation periods, the modelled prevailing wave direction at the outer wave buoy was around 225 degrees, and all waves with a height of 2 m or over came from direction between 175 and 225 degrees. The highest significant wave height
 85 of 2.9 m was during a wave event from 195 degrees with mean wave periods ($T_{m_{01}}$) up to 5.8 s. The simulation period also captured high waves (up to 1.7 m) from the east (95 deg), although these were less frequent. This distribution aligns with the dominant directions observed in the Gulf of Finland (Pettersson et al., 2010). Statistics of the modelled near-bottom velocities can be found in Appendix B.

We validated the modelled near-bottom orbital velocities and wave periods by determining them from the measured wave
 90 spectrum using the same water depth as in the bathymetrical grid used in SWAN. Near-bottom velocities were modelled accurately at both locations (Fig. 3a&c) with the more exposed outer location showing a -0.04 cm s^{-1} bias and 0.47 cm s^{-1} root-mean-square-error (RMSE). The slightly shallower inner location had a 0.08 cm s^{-1} bias and 0.49 cm s^{-1} RMSE. Modelled near-bottom periods (Fig. 3b&d) agreed well at the inner location with a 0.12 s bias and 0.88 s RMSE. For the outer location, bias was 2.23 s and RMSE 3.31 s , reflecting deeper water where wave orbital motions do not reach the bottom
 95 and the period is determined by low-frequency noise in the measurements. As seen in Fig. 3b, near-bottom periods were well modelled during high near-bottom velocities, but less defined under calm conditions. Overall, modelled wave data was sufficiently accurate for this study.

2.3 Wave-induced shear stress, τ_w

The near-bottom shear stress was computed as (e.g. Soulsby, 1997):

$$100 \quad \tau_w = 0.5\rho_w f_w U_{bot}^2, \quad (1)$$

where $\rho_w = 1003 \text{ kg m}^{-3}$ is the water density and f_w is the wave friction coefficient. The friction coefficient was determined following Soulsby (1997) as the higher of the rough and smooth bottom estimates:

$$f_w = \max\{f_{wr}, f_{ws}\}, \quad (2)$$

where

$$105 \quad f_{wr} = 0.237r^{-0.52}, \quad (3)$$

is the rough bottom friction coefficient, $r = a_{bot}/k_s$, $k_s = 2.5d_{50}$ is the Nikuradse equivalent sand grain roughness, and

$$f_{ws} = BR_w^{-N} \quad (4)$$

is the smooth bottom friction coefficient. Here $R_w = U_{bot}a_{bot}/\nu$ is the Reynolds number, ν is the kinematic viscosity of water ($1.3 \cdot 10^{-6} \text{ m}^2 \text{ s}^{-1}$), a_{bot} is the amplitude of the wave-induced near-bottom velocities (see Appendix A for a definition), and

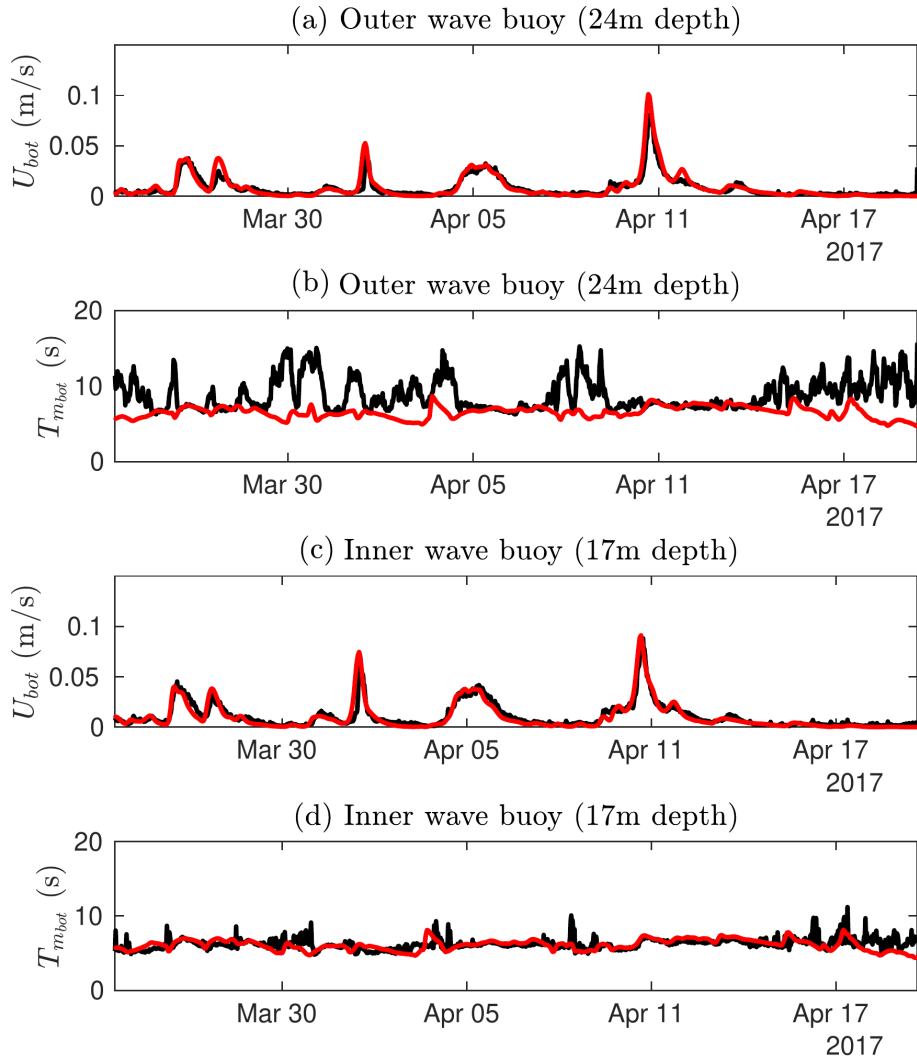


Figure 3. Wave-induced near-bottom orbital velocities and wave period calculated by the SWAN model (red) and the wave spectra measured by wave buoys (black).

110 B and N are constants that depend on the Reynolds number such that:

$$B = 2, N = 0.5 \text{ for } R_w \leq 5 \cdot 10^5 \text{ (laminar)} \quad (5)$$

$$B = 0.0521, N = 0.187 \text{ for } R_w > 5 \cdot 10^5 \text{ (turbulent)} \quad (6)$$

Table 1. The depth (m), median grain size d_{50} (μm), dry bulk density ρ_B (g cm^{-3}), Chlorophyll *a* ChlA ($\mu\text{g g}^{-1}$) and critical shear stresses, τ_{cr} (N m^{-2}) based on the in situ measurements. $\langle \rangle$ denotes averages, which have been calculated as means of monthly means.

Site	Depth	Type (in situ)	$\langle d_{50} \rangle$	$\langle \rho_B \rangle$	$\langle ChlA \rangle$	$\langle \tau_{cr} \rangle$
ID01	3.9	Mixed sediment	158	1.90	14.00	0.78
ID02	3.2	Sand	320	1.97	16.97	1.12
ID03	3.0	Mixed sediment	155	1.90	16.38	1.12
ID04	2.3	Mud	55	1.44	19.95	0.54
ID05	2.6	Sand	502	1.77	22.52	0.45
ID06	3.0	Sand	216	1.90	9.95	0.80
ID07	3.0	Sand	419	1.95	19.18	0.79
ID09	3.0	Mixed sediment	154	1.76	21.68	0.96
ID10	3.8	Sand	370	2.00	19.70	-
ID11	3.2	Sand	389	2.00	6.35	0.81
ID14	3.4	Sand	274	1.92	27.34	1.52
ID15	3.7	Mixed sediment	178	1.82	13.65	0.48
ID16	3.5	Mud	78	1.50	17.88	0.45

3 Environmental data and seabed classification

3.1 Environmental data

115 Environmental data and critical shear stress measurements were available from two field campaigns conducted in the years
2014 (Joensuu et al., 2018) and 2015 (Joensuu et al., 2020) in the Hanko archipelago. In 2014, samples were gathered from
16 shallow sites (depth < 4 m), covering a sedimentary gradient from mud to sand (median grain sizes 21–570 μm). These
sampling locations are illustrated in Fig. 2. The 2014 field campaign focused on spatial variation in sediment erodibility,
maximizing variation in sediment surface characteristics (e.g. bedforms, biofilms) across sites. In 2015, three sites (mud (ID04),
120 mixed (ID09), and sandy (ID14) sediment) from the 2014 study were re-sampled from April to December to capture temporal
variation in sediment erodibility. In this campaign, variation in sediment characteristics was minimized to focus solely on
temporal changes.

The sampling procedure was consistent across both campaigns. At each site, SCUBA divers collected samples by carefully
inserting EROMES cores (10 cm diameter, 10 cm depth) into the sediment (Schünemann and Köhl, 1991). Samples were
125 maintained at in situ temperatures and transported to the laboratory for further measurements. A total of 59 and 73 EROMES
cores were collected in 2014 and 2015, respectively. For a detailed description of the sampling procedures, see Joensuu et al.
(2018) and Joensuu et al. (2020). The grain size, dry bulk density and chlorophyll *a* for each measurement site were determined
from the combined 2014 and 2015 data as mean of monthly means (Table 1).

3.2 Measurements of critical shear stresses, $\hat{\tau}_{cr}$

130 In the 2014 and 2015 field campaigns (Joensuu et al., 2018, 2020), the critical shear stresses from the sediment samples were determined in the laboratory with a portable EROMES device (Schünemann and Kühl, 1991; Andersen, 2001). Bed shear stress on the sediment surface is generated by turbulent fluctuations induced by a propeller and baffle ring. The baffle ring prevents rotational flow and ensures turbulent flow fluctuations mimicking those observed by waves in nature. Suspended solids concentration is monitored with an OBS sensor (optical back-scattering sensor). The propeller revolutions have been
135 calibrated to nominal bed shear stresses (Schünemann and Kühl, 1991; Andersen, 2001).

At each run, the bed shear stress was increased every 2 min by 0.1 N m^{-2} from 0 to 2.0 N m^{-2} in the year 2014 study and from 0 to 1.6 N m^{-2} in the year 2015 study. Water samples for gravimetric analysis were collected during each run to calibrate the OBS sensor into suspended solids concentration (SSC; mg l^{-1}) (Andersen, 2001; Andersen and Pejrup, 2002). The critical shear stress (N m^{-2}) was defined at the erosion rate of $0.1 \text{ (g m}^{-2}\text{s}^{-1}\text{)}$, which describes the erosion after the
140 erosion of unconsolidated "fluffy" material (Andersen, 2001; Andersen et al., 2005). For a more extensive description of the laboratory procedures, see Joensuu et al. (2018, 2020).

Since the EROMES device is not reliable for large grain sizes, we excluded individual critical stress measurements when the median grain size of the sample exceeded $300 \mu\text{m}$. Consequently, no reliable measurements were obtained from site ID10 (Table 1).

145 3.3 Class-based seabed model

We used EMODnet Seabed Substrates (1:100k) (Kaskela et al., 2019) to define seabed classes: Mud to muddy sand, Sand, Mixed sediments, Coarse sediments, and Boulders (see Fig. 4a). Coarse sediments and Boulders were excluded from this study, since we had no in situ data from those seabed types. For Mud, Sand, and Mixed sediments we determined representative median grain sizes for each seabed type based on the data from Sect. 3.1 (Table 2). The representative values were determined
150 as means of monthly means to not give too much weight to data from the spatial campaign.

4 Models for critical shear stresses, τ_{cr}

4.1 Soulsby and Whitehouse (1997)

The critical value of the shear stress is the value that needs to be exceeded in order for resuspension to take place. The critical value depends on the sea floor properties, and is given by

$$155 \tau_{cr} = \theta_{cr}(\rho_s - \rho_w)gd_{50} \quad (7)$$

where τ_{cr} (N m^{-2}) is the critical shear stress, θ_{cr} is the threshold Shields parameter, g is the gravitational acceleration (9.82 m s^{-2}), ρ_s is particle density (2650 kg m^{-3}), ρ_w is the water density (1003 kg m^{-3}) and d_{50} is median grain size (m) (Soulsby, 1997).

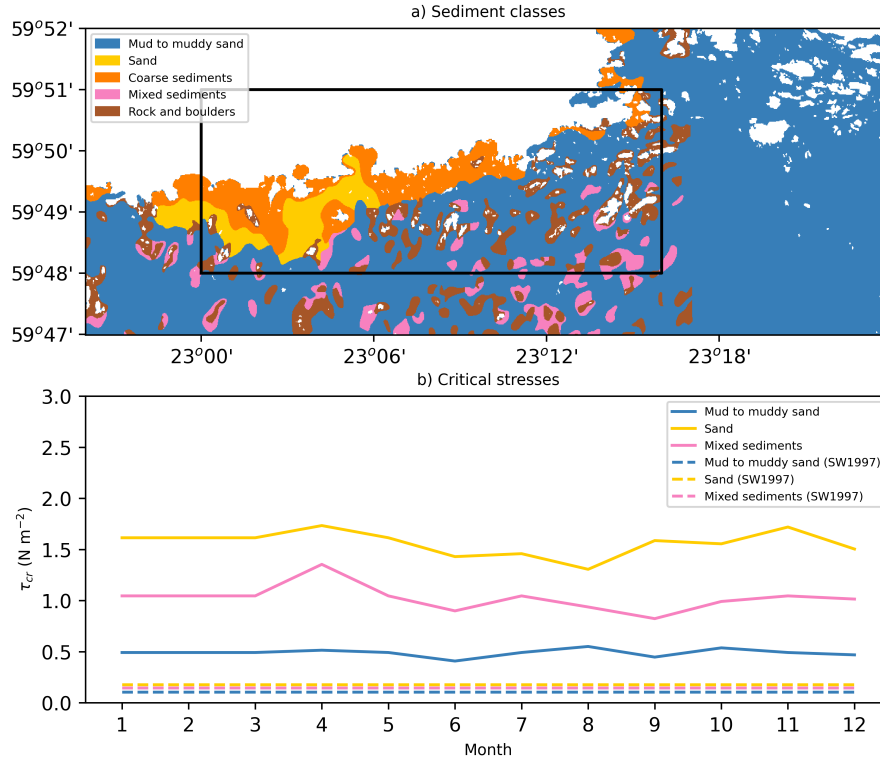


Figure 4. The sediment classes from the EMODnet data (a) and the critical shear stresses estimated based on the time varying model (Eq. 10) and the d_{50} model of Soulsby and Whitehouse (1997) (Eq. 7) (b). The black rectangle in (a) is the area shown in Figures 6–9.

The parametrization of the Shields parameter, as improved by Soulsby and Whitehouse (1997), reads:

$$160 \quad \theta_{cr} = \frac{0.3}{1 + 1.2D_*} + 0.055 \left[1 - \exp(-0.02D_*) \right] \quad (8)$$

where D_* is the dimensionless grain size calculated with

$$D_* = \left(\frac{g(\frac{\rho_s}{\rho_w} - 1)}{\nu^2} \right)^{\frac{1}{3}} d_{50}. \quad (9)$$

The strength of this model is its simplicity, but we found it to result in estimates of the critical stress that were an order of magnitude too small compared to values determined in the laboratory from in situ samples (Fig. 4b).

165 4.2 Thompson et al. (2019)

Thompson et al. (2019) developed predictive models for critical shear stress based on physical and biological characteristics in the Celtic Sea and North Sea. Their approach combined principal component analysis (PCA) and multiple linear regression, identifying key predictors such as median grain size, sorting, kurtosis, percentage of fines, bulk density, porosity, chlorophyll a , and organic carbon. Two models were proposed:

Table 2. Representative physical properties for each sediment class used in the model. The values for chlorophyll *a* is an average outside the growth season (growth season marked in bold), and is used if there is no month-specific value available.

Variable	Mud	Sand	Mixed sediments
d_{50} (μm)	59	284	169
ρ_B (g cm^{-3})	1.45	1.92	1.83
ChlA ($\mu\text{g/g}$)	19.48	29.58	21.57
January	–	–	–
February	–	–	–
March	–	–	–
April	20.28	33.83	32.55
May	–	–	–
June	16.50	23.01	16.35
July	–	24.05	–
August	21.58	18.60	17.71
September	17.88	28.60	13.65
October	21.10	27.48	19.63
November	–	33.32	–
December	18.66	25.66	20.46

170 Model 1 (Celtic Sea): Included both physical and biological parameters, suggesting that bed stability increases with grain size, better sorting, and higher bulk density, while decreasing with higher fines and organic carbon.

Model 2 (North Sea): Relied on physical parameters only, but over-predicted bed strength when applied to Celtic Sea data.

175 These models demonstrated that physical characteristics dominate bed stability, while biological factors (e.g. chlorophyll *a*) play a secondary role. However, they also highlighted the complexity and co-variation of sediment properties, making broad-scale predictions challenging without site-specific data.

180 These models were not applicable in our study for several reasons. First, we lacked key parameters such as grain sorting and kurtosis, and organic carbon content, which are essential for Model 1. Second, the model had a negative coefficient for dry bulk density despite Figure 3 of Thompson et al. (2019) showing a positive relationship between bulk density and bed stability. This negative coefficient combined with bulk densities being higher in our data compared to the dataset of Thompson et al. (2019), resulted in unphysical values of the critical shear stress. Finally, their models were calibrated for Celtic and North Sea conditions, which differ from our study area in water depth, sediment composition, hydrodynamic forcing, and stress history.

4.3 A non-stationary physical–biological model

We constructed a parsimonious model that couples time-invariant physical factors – median grain size (d_{50} , μm) and dry bulk density (ρ_B , g cm^{-3}) – with a time-varying biological proxy, chlorophyll a (ChlA, $\mu\text{g g}^{-1}$). To fit the model we went back to the raw data obtained from the in situ measurements reported by Joensuu et al. (2018, 2020). Since EROMES measurements are not reliable for very coarse sands, samples with $d_{50} > 300 \mu\text{m}$ were excluded.

The model was determined as a three variable least-squares fit using the individual samples from the raw data. In other words, the model predicts critical shear stress as:

$$\tau_{cr} = \beta_0 + \beta_1 d_{50} + \beta_2 \rho_B + \beta_3 \text{ChlA} \quad (10)$$

where τ_{cr} is critical shear stress (N m^{-2}), β_0 is intercept, d_{50} is median grain size (μm), ρ_B is dry bulk density in (g cm^{-3}), and ChlA is chlorophyll a ($\mu\text{g g}^{-1}$).

The fit made to each of the classes (Sand, Mud, Mixed sediments) separately had a modest predictive power, but a fit to all the data shows that the model can predict especially the variation between the classes (Table 3, Fig. 5). For the purpose of applying the model to the seabed classes from Sect. 3.3, the variation between classes is the most important property for the model.

While physical variables explained most of the variation in τ_{cr} , adding chlorophyll a as a variable increased the R^2 by approximately 0.1. We also note that d_{50} and ρ_B were strongly correlated ($R = 0.86$), while ChlA was weakly correlated with the physical variables ($R = 0.10 - 0.34$).

Table 3. The models for the critical shear stress $\tau_{cr} = \beta_0 + \beta_1 d_{50} + \beta_2 \rho_B + \beta_3 \text{ChlA}$ (Eq. 10) based on data from Joensuu et al. (2018, 2020). The fit to data of all types (bold) is the one used in this study.

Sediment type	β_0 (N m^{-2})	β_1 ($\text{N m}^{-2} (\mu\text{m})^{-1}$)	β_2 ($\text{N m}^{-2} (\text{g cm}^{-1})^{-1}$)	β_3 ($\text{N m}^{-2} (\mu\text{g g}^{-1})^{-1}$)	R^2
All types	-1.027	0.003	0.568	0.028	0.659
Mud	-0.825	0.002	0.450	0.030	0.144
Sand	-3.967	0.004	2.039	0.022	0.286
Mixed sediments	-1.206	0.001	0.734	0.033	0.418

Our aim was not to build the most comprehensive model for the τ_{cr} but to define a practical model that can be combined with numerical wave model outputs. To use the modelled critical shear stresses to the spatio–temporal wave model data, we need to determine representative values of d_{50} and ρ_B for each of the three classes (Mud, Sand, and Mixed sediments), and monthly values of ChlA for each of the classes. The model is not applied to coarse sediments or boulders because representative values cannot be reliably determined from the available data.

The raw data from the in situ samples were therefore grouped according to the determined seabed classes: Mud = {ID04, ID16}, Sand = {ID02, ID05, ID06, ID07, ID10, ID11, ID14} and Mixed = {ID01, ID03, ID09, ID15} (see Table 1). For each

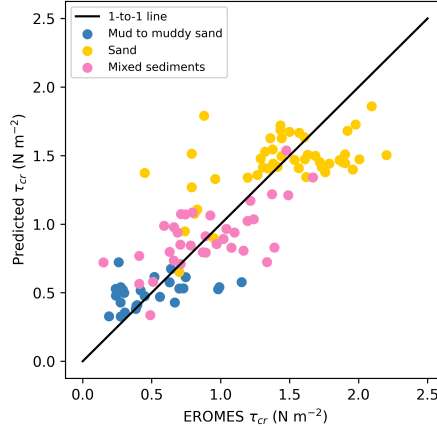


Figure 5. The critical stresses determined with the EROMES device from in situ samples compared to the critical stresses predicted using d_{50} , ρ_B and ChlA (Eq. 10)

site, monthly means were computed while retaining the year (e.g. 08-2014 and 08-2015 remain distinct) to avoid overweighting data from the spatial campaign. For d_{50} and ρ_B , class-level monthly means were computed and then averaged to obtain time-invariant values (Table 2). For ChlA , temporal variability was retained by computing monthly means for each class. Months lacking measurements were filled with the off-season mean (September–April).

210 The physical variables (d_{50} and ρ_B) defines the overall magnitude of the critical stress for each class, with Mud being lowest, and Sand being highest (Fig. 4b). The variation caused by the monthly variations in ChlA is significant (Table 4), being up to 52% of the mean value for Mixed sediments, and 29% and 27 % for the Sand and Mud respectively. Nevertheless, the monthly variation never changes the ordering between the classes.

Table 4. The critical stresses $\tau_{cr}(d_{50}, \rho_B, \text{ChlA}(t))$ modelled using the non-stationary physical–biological model (Eq. 10) and the values determined from the data of Joensuu et al. (2018, 2020) (Table 2). $\langle \rangle$ denotes the average of all the monthly values.

Sediment type	$\langle \tau_{cr} \rangle$	$\min(\tau_{cr})$	$\max(\tau_{cr})$
Mud	0.49	0.41	0.55
Sand	1.56	1.31	1.73
Mixed sediments	1.02	0.82	1.35

5 Spatially extensive wave-induced shear stresses

215 5.1 Numerical model results

Modelled shear stresses were estimated based on the near-bottom velocities (Sec. 2.2), the representative grain sizes (Sec. 4.3), and the friction coefficients (Sec. 2.3). The shear stresses were determined for every model time step from all available data (2014, 2015 and 2017). The in situ data doesn't contain samples from categories Boulders or Coarse sediments. Therefore, no representative grain sizes could be determined, and wave-induced near-bottom stresses could not be determined. Results are therefore only given for categories Mud, Sand and Mixed sediments, while the other areas are masked out.

220 Mean values were generally low, remaining below 1 N m^{-2} across the entire area (Fig. 6a). The 95th percentiles are between 0.5 and 1 N m^{-2} for larger areas, especially where the bottom type was classified as sand, and even exceeding 1 N m^{-2} for smaller areas (Fig. 6b). While the areas with sand bottom are highlighted also in the maximum shear stress values, the highest values (exceeding 2 N m^{-2}) can be found at mud bottoms. These high values are caused by high near bottom velocities in the exposed area (see Fig. A1). The maximum values indicate that the area directly south-west of the Tvärminne research station is well sheltered from waves, resulting in low wave-induced near-bottom shear stresses.

5.2 Exceedance probabilities for critical shear stress

Modelled near-bottom shear stresses were compared to critical shear stresses to estimate resuspension exceedance probabilities. These probabilities reflect the likelihood that wave-induced shear stress exceeds the critical value, indicating potential sediment resuspension. Exceedance depends on wave conditions, depth, and seabed class. The critical threshold was determined from the model in Sect. 4.3, and therefore varied monthly. Exceedance probabilities were determined simply from the fraction of times the modelled shear stress for a given time exceeded the modelled critical shear stress for the given class and month. The model is not applicable to categories Boulders and Coarse sediments, and those areas are therefore masked out.

235 Exceedance of the critical shear stress threshold was generally low across the study area (Fig. 7). Localized patches in the outer archipelago exhibited exceedance of up to 10%, indicating that sediment mobilization mostly occurs during episodic high-energy events. These areas were not limited to the coastline but also appeared among groups of islands and islets located about 2–3 km from the shoreline where the water is shallow, and includes narrow channels that concentrate wave energy. Sheltered nearshore areas remained below the threshold, suggesting stable sediments and minimal resuspension potential. Even during high-wind events, modeled wave-induced shear stresses rarely exceeded predicted or measured thresholds, indicating that sediment mobilization is episodic and limited to localized areas.

240 Kahma (2021) estimated the potential for wave-induced near-bottom velocities using the long-wave (7 s) wave heights from a ray-tracing model as a proxy. The results of Kahma (2021) were 10% exceedance values. While they are able to identify some areas that might be vulnerable to higher wave-induced near-bottom velocities, the author noted that they are not a substitute for specifically modelling the near-bottom velocities. The use of wave heights as a proxy can naturally also not account for the variation in the seabed type or the temporal variation of the critical stress caused by changing biological activity, as done in this study.

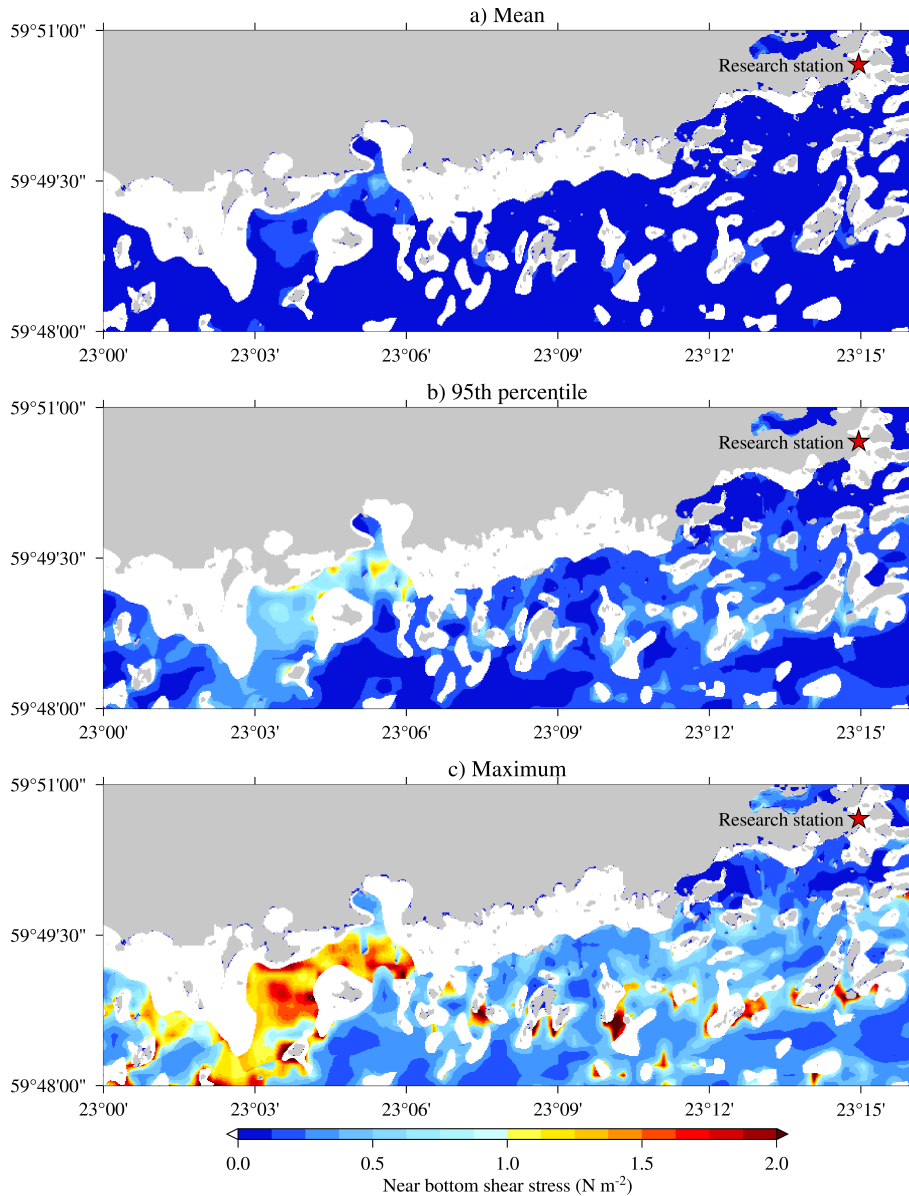


Figure 6. The mean (a), 95th percentile (b), and maximum values (c) of the modelled near-bottom shear stress for all the available model data. No results are available for classes Boulders and Coarse sediments (white), since no measurements were available from those classes to determine representative grain sizes. The red star marks the Tvärminne research station for reference.

5.3 Wave-induced stresses during representative high-wind events

Two late-November 2015 storms illustrate the impact of strong winds on wave forcing and sediment resuspension. On 28 November, south-westerly winds ($19\text{--}20\text{ m s}^{-1}$) generated significant wave heights of $\sim 3\text{ m}$ offshore and $\sim 2\text{ m}$ within the

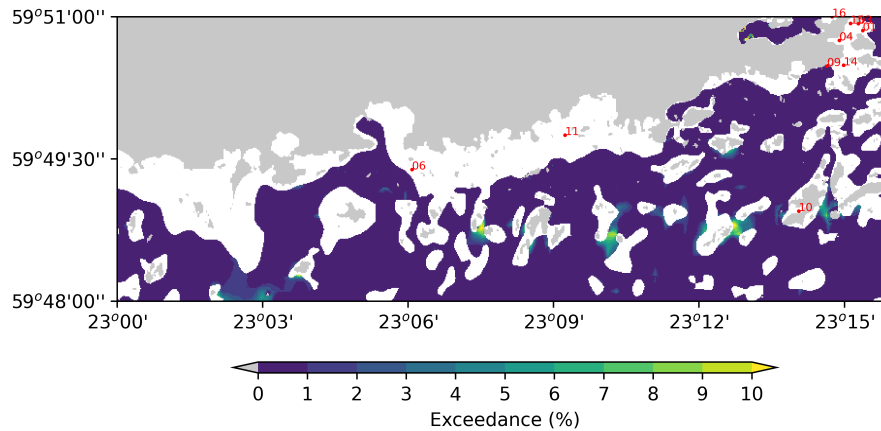


Figure 7. Percent of times the modelled shear stresses exceeded the modelled critical values. No results are available for classes Boulders and Coarse sediments (white), since no measurements were available from those classes to determine representative values for grain size, dry bulk density and chlorophyll *a*.

250 archipelago (Fig. 8a). Near-bottom orbital velocities reached 0.5 m s^{-1} along exposed coastlines (Fig. 8b), producing localized shear stresses exceeding 2 N m^{-2} (Fig. 8c).

The 30 November event was more severe, with SSE winds of $23\text{--}25 \text{ m s}^{-1}$ (gusts up to 26 m s^{-1}) causing offshore wave heights beyond 4 m and near-bottom velocities approaching 1 m s^{-1} in shallow exposed areas (Fig. 9b). Shear stresses surpassed 2 N m^{-2} across extensive outer archipelago areas, conditions sufficient to mobilize coarse sediments and cause
 255 widespread resuspension (Fig. 9c).

While the highest shear stresses were mostly concentrated to the same areas in both cases, the areas with sand bottom in the western part of the area were more exposed during the SSE winds on 30 November. These two examples represent typical cases of higher waves propagating towards the shore, with south-westerly winds being the most dominant in the area. Together these two events demonstrate that sediment mobilization is highly episodic, concentrated in exposed shallow areas and constricted
 260 channels, with implications for turbidity, nutrient fluxes, and benthic habitats.

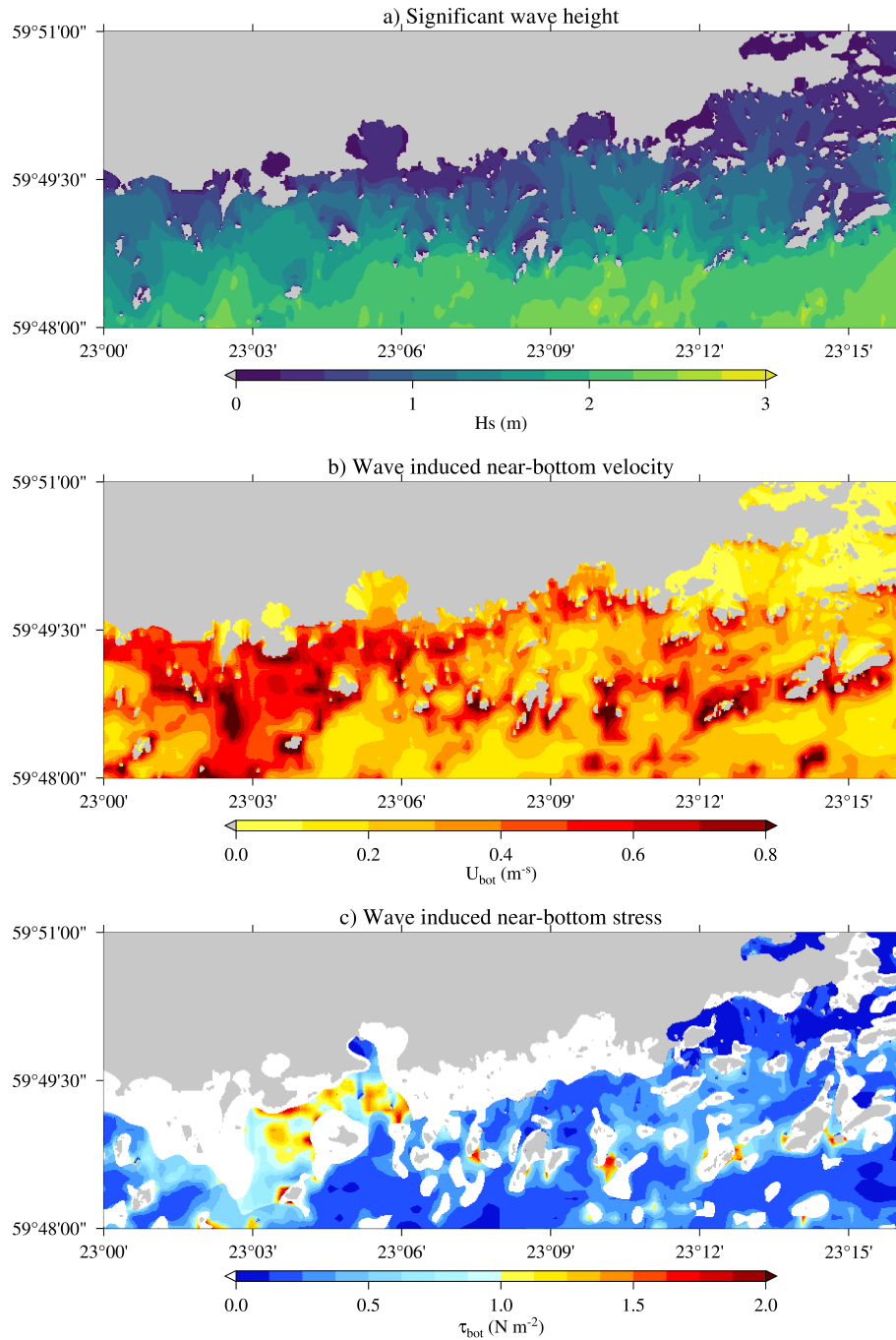


Figure 8. Wave conditions on 28 November 2015 during SW winds: (a) significant wave height, (b) near-bottom orbital velocity, (c) shear stress. Near bottom stresses are not available for classes Boulders and Coarse sediments (white), since no measurements were available from those classes to determine representative grain sizes.

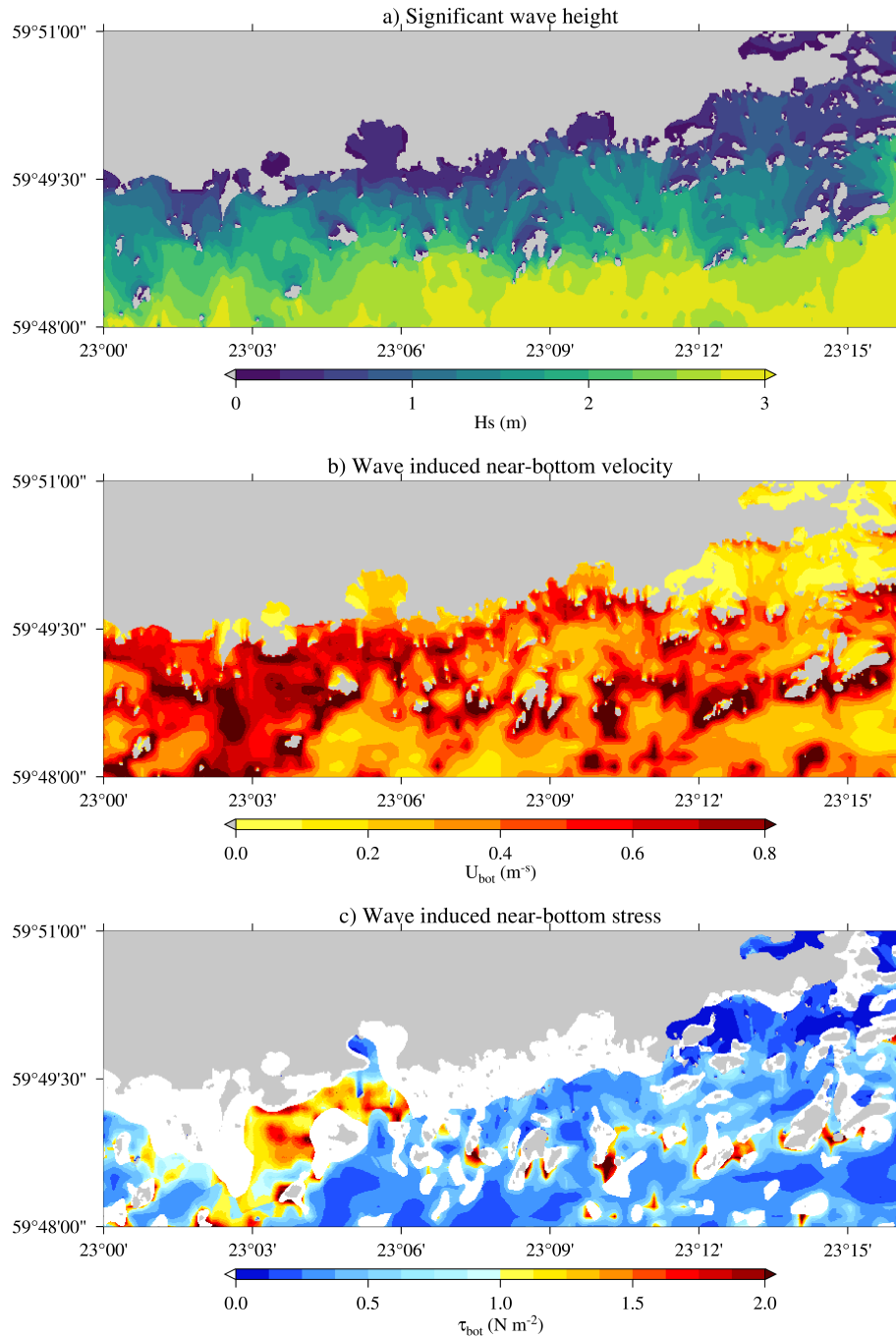


Figure 9. Wave conditions on 30 November 2015 during SSE winds: (a) significant wave height, (b) near-bottom orbital velocity, (c) shear stress. Near bottom stresses are not available for classes Boulders and Coarse sediments (white), since no measurements were available from those classes to determine representative grain sizes.

6 Discussion

The erodibility of natural sediments is influenced by a complex interplay of physical, geochemical, and biological sediment properties. For example, benthic fauna can modify sediment erodibility by altering water content, bulk density, and the particle size distribution through bioturbation activities (de Deckere et al., 2001; Le Hir et al., 2007). The experimental critical shear stresses used in this study were derived from natural submerged sediment samples, capturing variability across both space (Joensuu et al., 2018) and time (Joensuu et al., 2020). The theoretical grain-size-based thresholds following Soulsby and Whitehouse (1997) underestimated the sediment stability of the data by Joensuu et al. (2018, 2020) by roughly an order of magnitude. Indeed, previous work by e.g. Thompson et al. (2019) has shown that bulk density is an important parameter when predicting the critical shear stress, while also incorporating more detailed information about the grain size distribution (e.g. kurtosis).

Our data did not contain detailed information about the grain size distribution, so unfortunately we could not apply the models of Thompson et al. (2019) directly, but we could only assume some typical values for the missing parameters. We still found that the models of Thompson et al. (2019) were not a good description for our data. One of the main issues was that the dependence on the bulk density was negative when using multiple variables, even though the authors had found a positive dependence when using only the bulk density to describe the critical stresses (see their Figure 3). It would seem like the model did not extrapolate well to the higher values of bulk density in our data. This discrepancy in sign for the coefficient might have been caused by correlations between the used variables, but we did not investigate the causes in more detail. Another reason for the weak predictive power of the model by Thompson et al. (2019) to our data might be the biological activity that can vary strongly with depth, and our data were collected in a much shallower region.

The primary limitation of grain-size-only models is their inability to account for consolidation and biological effects. Bulk density is a strong predictor of sediment stability: high-density sediments are more compacted and resistant to erosion, whereas low-density sediments are loose and easily mobilized. Biological activity further modifies stability, especially throughout the growth season, complicating critical shear stress estimates and spatial mapping. We therefore proposed a model that addresses these limitations by incorporating bulk density and chlorophyll *a* as a proxy for biostabilization.

We decided to build our model that relies on a few key variables for two main reasons. First, a model can only be applied if the necessary data is available. Using only three variables increases the likelihood that future datasets will contain all the required variables. Second, many of the variables correlate, and using several correlated variables further increases the uncertainty in the estimates for the individual coefficients when working with a limited data set. We chose to fit our model to three parameters: median grain size, dry bulk density and chlorophyll *a*. The physical aspects are covered by the grain size and bulk density, while the biology is represented by the chlorophyll *a*. There are no objective way to choose the variables, but these three have been used in previous models and it is expected that they might be among the variables that are more routinely measured compare to e.g. grain size distributions.

The three parameter linear model could explain most of the variation of the measured shear stresses between the classes (Mud, Sand, and Mixed sediments) (Fig. 5). Nonetheless, the variation of the individual critical stress measurements from

295 the data within a single class were not explained equally well (Table 3). The model especially struggled with samples from a
muddy seafloor, while performing better on samples classified as mixed sediments. Joensuu et al. (2020) found that, compared
to the other classes, the shear stress for muddy bottoms were more heavily influenced by the biology, and we surmise that a
single variable (ChlA) might not be enough to capture the biological effects well enough to sufficiently model the variations
in critical stress on muddy seabeds. Nonetheless, if the aim is to generalize the measurements spatially with only class-based
300 maps, each class can only be represented by a single value. It is therefore most critical that the model can separate the varying
behaviour between the classes. It follows, however, that if spatial maps with more detailed information would be available,
they would simultaneously increase the requirements on the model for the critical shear stress.

Our study highlights that bridging the gap between single in situ measurements and larger scale numerical simulations
is far from straightforward. One of the largest uncertainties seems to be the classification of the seabed types and finding
305 representative values for the classes. The combination of our measurements with the EMODnet seabed model had two main
weaknesses: 1) Our in situ data could not provide representative values for all of the classes. While areas covered with boulders
are not relevant from a resuspension perspective, lacking results of the large areas marked as coarse sediments near the coastline
is a clear limitation. 2) The classification doesn't seem to properly match up with the bottom types determined from the in situ
samples. Several stations that had been determined as sand from the samples were located in the coarse sediment category in
310 the EMODnet data.

A second, although probably lesser, source of uncertainty lies in the bottom depth and wave model simulation itself. The
water depth used in the wave model directly influences the results, as surface waves are affected by factors like bottom friction
and wave breaking, both of which depend on local water depth. More critically, the water depth is essential for transferring
surface wave energy to the bottom, as wave motion attenuates rapidly with depth. This sensitivity is evident from wave mea-
315 surements made with the inner wave buoy, where the water depth is approximately 17 metres; if a 15 meter depth is used to
transfer the measured surface waves to the seafloor, the mean orbital velocities increase by 26% (not shown). Nevertheless, the
sensitivity to small discrepancies in the water depth should decrease in extremely shallow depths, as horizontal wave motion
does not attenuate significantly when the wavelength is at least 20 times the water depth. Furthermore, accurate estimates of
near-bottom mean currents were not available for this study, and the absence of current data likely biases the resuspension
320 probabilities toward lower values. Nevertheless, current speeds are expected to be relatively low compared to the maximum
wave-induced velocities, especially since tidal currents in the the Baltic Sea are generally weak.

Overall, sediment resuspension potential is highly heterogeneous in the Hanko archipelago. Even with accurate wave forcing
simulations, exceedance probabilities should be interpreted qualitatively until larger datasets and regional calibration reduce
uncertainty. Future work should expand empirical measurements, incorporate biological metrics, and test model transferability
325 across regions.

7 Conclusions

We implemented a numerical spectral wave model (SWAN) with an exceptionally high spatial resolution (20 m) for the coastal archipelago area of Hanko in the Baltic Sea. Modeled wave-induced shear stresses were combined with seabed data to estimate potentials for sediment resuspension and compared against laboratory-derived critical shear stresses from in situ samples.

330 Our results reveal a strong spatial variability in near-bottom orbital velocities and shear stresses, driven by depth gradients and exposure differences. Nevertheless, theoretical critical shear stresses based on grain size alone underestimate sediment stability. To address this limitation, we developed a parsimonious predictive model that integrates grain size, bulk density, and seasonal chlorophyll *a* as a proxy for biostabilisation. The model was found to be relatively accurate to predict critical shear stresses between sediment classes, and was therefore well suited to be used with the class-based spatial maps available for our
335 study area.

Our model could predict a significant seasonal variation in the critical shear stress based on the the seasonal chlorophyll *a* values, thus highlighting the importance of including the biological activity when modelling the critical shear stress. At the same time it is not obvious how to best model the effect of the biological activity, especially on a more detailed level than the class based monthly values used in this study. Our findings in comparing our data to previously published models for critical
340 shear stress also suggests that applying these type of locally determined models to other geographical areas might be extremely challenging, if even feasible.

This study underlines the importance of incorporating both physical and biological factors – and their temporal dynamics – into sediment transport models to achieve reliable predictions of erosion thresholds and resuspension potential. Additional work is still required to construct models that can reconcile data from different geographical areas and conditions, and that can
345 accurately predict the observed spatio-temporal variations in critical shear stress both between in within seabed classes. Such improvements would be of significant support to coastal management and ecosystem restoration.

Code and data availability. The seabed data can be accessed through <https://www.emodnet-geology.eu/data-products/seabed-substrates/>. The open source SWAN model can be downloaded at <https://swanmodel.sourceforge.io/>. The wave buoy data is archived in a repository (Björkqvist et al., 2025) and will be opened upon the acceptance of the manuscript. The sediment data from 2014 and 2015 are archived in a
350 repository (Savela, 2025) and will be opened upon the acceptance of the manuscript.

Appendix A: Definition of wave parameters

Third generation numerical wave models model the so called wave spectrum $S(\omega)$ (m^2s), which gives the variance density of waves of different (angular) frequency $\omega = 2\pi f$ (rad s^{-1}) and direction, θ (rad), where f (Hz) is the linear frequency. The variance of a wave component is directly proportional to the square of its height, which is directly proportional to its energy.

355 The wave model solves the action balance equation, not the energy balance equation, since the spectral variance density is only conserved in deep water without currents. Since this study did not use currents, we give the action balance equation (e.g. Holthuijsen, 2007) below without currents:

$$\frac{\partial N}{\partial t} + \nabla_{\mathbf{x}} \cdot (c_g N) + \frac{\partial c_\sigma N}{\partial \sigma} + \frac{\partial c_\theta N}{\partial \theta} = \frac{G_{tot}}{\sigma}, \quad (\text{A1})$$

360 where $N = S/\sigma$ is the wave action, c_g is the group speed of a wave component, c_σ and c_θ signifies the speed of the change in frequency and direction, $\nabla_{\mathbf{x}}$ is the spatial partial derivative, and G_{tot} is a sum of the so called source terms, which model the different physical processes that add, remove or redistribute energy of the wave components. Without currents the intrinsic frequency σ (rad s⁻¹) equals the angular frequency ω .

The wave parameters were calculated from the modelled or measured wave spectrum. First, the near-bottom wave spectrum was calculated (The SWAN team, 2024):

$$365 \quad S_b(\omega) = \frac{S(\omega)}{\sinh^2 kh}, \quad (\text{A2})$$

where $S(\omega)$ (m²s) is the aforementioned surface wave spectrum, h (m) is the water depth, and k (rad m⁻¹) is the wavenumber solved from wave frequency using linear wave theory. Note, that the wave spectrum from both wave measurements and model output is usually given as a function of f , and in this case $E(f) = 2\pi S(\omega)$ (m²Hz⁻¹) to conserve the area under the spectral curve (i.e. the total variance of the wave field).

370 The maximum near-bottom orbital velocity U_{bot} (m s⁻¹) is defined (The SWAN team, 2024) using the near-bottom spectrum as

$$U_{bot} = \sqrt{2 \int S_b(\omega) \omega^2 d\omega} = \sqrt{2} U_{rms}, \quad (\text{A3})$$

where U_{rms} is the root-mean-square orbital velocity at the bottom.

The near-bottom amplitude a_{bot} (m) is defined as

$$375 \quad a_{bot} = \sqrt{2 \int S_b(\omega) d\omega}, \quad (\text{A4})$$

while the near-bottom mean wave period is defined as

$$T_{m_{bot}} = 2\pi \sqrt{\frac{\int S_b(\omega) d\omega}{\int S_b(\omega) \omega^2 d\omega}} = \sqrt{\frac{\int E_b(f) df}{\int E_b(f) f^2 df}}. \quad (\text{A5})$$

The relationship between these three parameters is therefore

$$a_{bot} = \frac{T_{m_{bot}} U_{bot}}{2\pi}, \quad (\text{A6})$$

380 meaning that two of them exactly determines the third.

Appendix B: Near-bottom velocities, U_{bot}

Figure A1 shows the mean, 95th percentile and max values of the modelled near-bottom velocities. These velocities are based purely on the wave model data, and don't contain any effects from the chosen grain sizes.

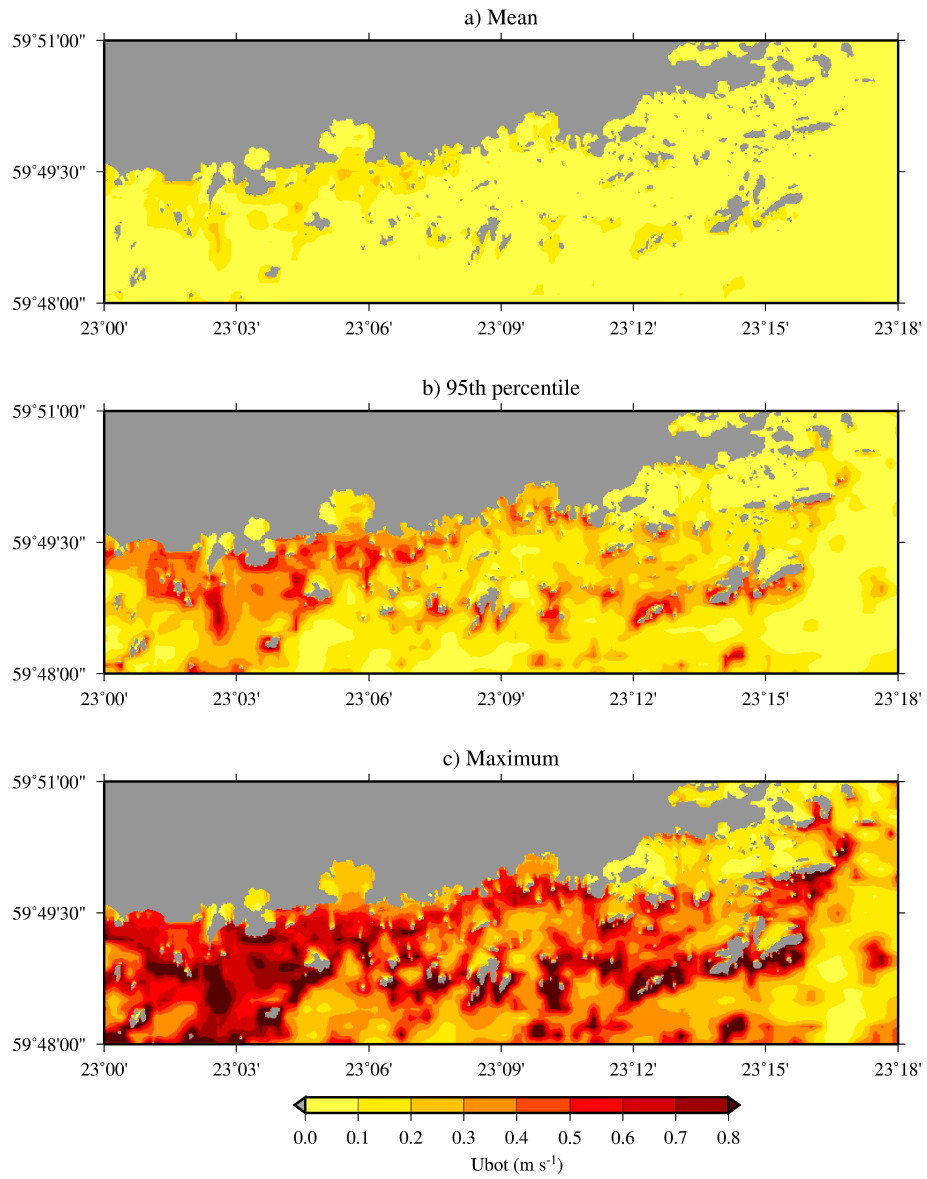


Figure A1. Near-bottom velocities (U_{bot}) as modelled by the SWAN model.

Author contributions. The study was initiated by MS and AN, and further conceptualized by MS, AN, HP and JVB. Majority of the sediment
385 samples were collected by AN and analyzed by MS. The critical shear stresses from the samples were determined by MS. The wave model
simulations were performed by VA and processed by JVB. The theoretical shear stresses were determined by HP and JVB, and the new
model for the shear stress was constructed by MS and JVB. The wave measurements were processed by JVB. The manuscript was prepared
by JVB and MS with contributions from all authors.

Competing interests. The authors declare that they have no competing interests.

390 *Acknowledgements.* Data used in this publication was made available by the EMODnet Geology project, <http://www.emodnet-geology.eu>
funded by the European Commission Directorate General for Maritime Affairs and Fisheries. These data were collected by the Geological
Survey of Finland. We thankfully acknowledge the work by Mr Kimmo Tikka to process the bathymetrical data used to construct the wave
model grid and the FMI technical staff in deploying and retrieving the wave buoys. This project got funding from Walter and Andrée de
Nottbeck Foundation and Onni Talas Foundation (MS). We are also grateful for two anonymous reviewers for constructive comments that
395 improved the manuscript.

References

- Abdolali, A., Roland, A., van der Westhuysen, A., Meixner, J., Chawla, A., Hesser, T. J., Smith, J. M., and Sikiric, M. D.: Large-Scale Hurricane Modeling Using Domain Decomposition Parallelization and Implicit Scheme Implemented in WAVEWATCH III Wave Model, *Coastal Engineering*, 157, 103–656, <https://doi.org/10.1016/j.coastaleng.2020.103656>, 2020.
- 400 Alari, V. and Raudsepp, U.: Simulation of Wave Damping Near Coast due to Offshore Wind Farms, *Journal of Coastal Research*, 28, 143–148, <https://doi.org/10.2112/JCOASTRES-D-10-00054.1>, 2012.
- Alenius, P., Myrberg, K., and Nekrasov, A.: The physical oceanography of the Gulf of Finland: a review, *Boreal Environ. Res.*, 3, 97–125, 1998.
- Andersen, T.: Seasonal variation in erodibility of two temperate, microtidal mudflats, *Estuarine, Coastal and Shelf Science*, 53, 1–12, 2001.
- 405 Andersen, T. J. and Pejrup, M.: Biological Mediation of the Settling Velocity of Bed Material Eroded from an Intertidal Mudflat, the Danish Wadden Sea, *Estuarine, Coastal and Shelf Science*, 54, 737–745, <https://doi.org/10.1006/ecss.2001.0856>, 2002.
- Andersen, T. J., Lund-Hansen, L. C., Pejrup, M., Jensen, K. T., and Mouritsen, K. N.: Biologically induced differences in erodibility and aggregation of subtidal and intertidal sediments: a possible cause for seasonal changes in sediment deposition, *Journal of Marine Systems*, 55, 123–138, <https://doi.org/10.1016/j.jmarsys.2004.09.004>, 2005.
- 410 Björkqvist, J.-V., Pettersson, H., and Roine, T.: Wave buoy data from the Tvärminne area from 2017, <https://doi.org/10.5281/zenodo.15781282>, 2025.
- Black, K. S., Tolhurst, T. J., Paterson, D. M., and Hagerthey, S. E.: Working with Natural Cohesive Sediments, *Journal of Hydraulic Engineering*, 128, 2–8, [https://doi.org/10.1061/\(ASCE\)0733-9429\(2002\)128:1\(2\)](https://doi.org/10.1061/(ASCE)0733-9429(2002)128:1(2)), 2002.
- Booij, N., Ris, R., and Holthuijsen, L. H.: A third-generation wave model for coastal regions 1. Model description and validation, *Journal of Geophysical Research*, 104, 7649–7666, <https://doi.org/10.1029/98jc02622>, 1999.
- 415 Dade, W. B., Nowell, A. R. M., and Jumars, P. A.: Predicting erosion resistance of muds, *Marine Geology*, 105, 285–297, [https://doi.org/10.1016/0025-3227\(92\)90194-M](https://doi.org/10.1016/0025-3227(92)90194-M), 1992.
- Datawell, BV: Datawell Waverider Manual, https://datawell.nl/wp-content/uploads/2024/09/datawell_manual_dwr4_2024-09-23.pdf, last accessed: 04.11.2025, 2024.
- 420 Datawell, BV: Datawell Waverider Reference Manual, https://datawell.nl/wp-content/uploads/2025/01/datawell_manual_dwr-mk3_dwr-gwr-sg_2025-01-08.pdf, last accessed: 04.11.2025, 2025.
- de Deckere, E. M. G. T., Tolhurst, T. J., and de Brouwer, J. F. C.: Destabilization of Cohesive Intertidal Sediments by Infauna, *Estuarine, Coastal and Shelf Science*, 53, 665–669, <https://doi.org/10.1006/ecss.2001.0811>, 2001.
- Decho, A. W.: Microbial biofilms in intertidal systems: an overview, *Continental Shelf Research*, 20, 1257–1273, [https://doi.org/10.1016/S0278-4343\(00\)00022-4](https://doi.org/10.1016/S0278-4343(00)00022-4), 2000.
- 425 Edge, K. J., Dafforn, K. A., Simpson, S. L., Ringwood, A. H., and Johnston, E. L.: Resuspended contaminated sediments cause sublethal stress to oysters: A biomarker differentiates total suspended solids and contaminant effects, *Environmental Toxicology and Chemistry*, 34, 1345–1353, <https://doi.org/10.1002/etc.2929>, 2015.
- Eerola, K.: Twenty-One Years of Verification from the HIRLAM NWP System, *Weather and Forecasting*, 28, 270–285, <https://doi.org/10.1175/WAF-D-12-00068.1>, 2013.
- 430 Grabowski, R. C., Droppo, I. G., and Wharton, G.: Erodeability of cohesive sediment: The importance of sediment properties, *Earth-Science Reviews*, 105, 101–120, <https://doi.org/10.1016/j.earscirev.2011.01.008>, 2011.

- Green, M. O. and Coco, G.: Review of wave-driven sediment resuspension and transport in estuaries, *Reviews of Geophysics*, 52, 77–117, <https://doi.org/10.1002/2013RG000437>, 2014.
- 435 Harris, R. J., Pilditch, C. A., Hewitt, J. E., Lohrer, A. M., Van Colen, C., Townsend, M., and Thrush, S. F.: Biotic interactions influence sediment erodibility on wave-exposed sandflats, *Marine ecology progress series*, 523, 15–30, 2015.
- Heiskanen, A.-S.: Factors governing sedimentation and pelagic nutrient cycles in the northern Baltic Sea, Ph.D. thesis, University of Helsinki, Helsinki, <https://jyu.finna.fi/Record/jykdok.759971>, doctoral dissertation, summary part, 1998.
- Holthuijsen, L. H.: *Waves in Oceanic and Coastal Waters*, Cambridge University Press, Cambridge, <https://doi.org/10.1017/CBO9780511618536>, 2007.
- 440 Joensuu, M., Pilditch, C. A., Harris, R., Hietanen, S., Pettersson, H., and Norkko, A.: Sediment properties, biota, and local habitat structure explain variation in the erodibility of coastal sediments, *Limnology and Oceanography*, 63, 173–186, <https://doi.org/10.1002/lno.10622>, 2018.
- Joensuu, M., Pilditch, C. A., and Norkko, A.: Temporal Variation in Resuspension Potential and Associated Nutrient Dynamics in Shallow Coastal Environments, *Estuaries and Coasts*, 43, 1361–1376, <https://doi.org/10.1007/s12237-020-00726-z>, 2020.
- Kahma, K. K.: Wind-generated long wave climate in the Tvärminne area, *Geophysica*, 56, 29–37, 2021.
- Kaskela, A. M., Kotilainen, A. T., Alanen, U., Cooper, R., Green, S., Guinan, J., van Heteren, S., Kihlman, S., Van Lancker, V., Stevenson, A., and the EMODnet Geology Partners: Picking Up the Pieces—Harmonising and Collating Seabed Substrate Data for European Maritime Areas, *Geosciences*, 9, <https://doi.org/10.3390/geosciences9020084>, 2019.
- 450 Koch, E. W., Ackerman, J. D., Verduin, J., and van Keulen, M.: Fluid Dynamics in Seagrass Ecology—from Molecules to Ecosystems, in: *Seagrasses: Biology, Ecology and Conservation*, Springer, Dordrecht, https://doi.org/10.1007/978-1-4020-2983-7_8, 2007.
- Le Hir, P., Monbet, Y., and Orvain, F.: Sediment erodability in sediment transport modelling: Can we account for biota effects?, *Continental Shelf Research*, 27, 1116–1142, <https://doi.org/10.1016/j.csr.2005.11.016>, 2007.
- Madsen, J., Chambers, P., James, W., Koch, E., and Westlake, D.: The interaction between water movement, sediment dynamics and submersed macrophytes, *Hydrobiologia*, 444, 71–84, <https://doi.org/10.1023/A:1017520800568>, 2001.
- 455 Michaud, E., Desrosiers, G., Mermillod-Blondin, F., Sundby, B., and Stora, G.: The functional group approach to bioturbation: II. The effects of the *Macoma balthica* community on fluxes of nutrients and dissolved organic carbon across the sediment–water interface, *Journal of Experimental Marine Biology and Ecology*, 337, 178–189, 2006.
- Miettunen, E.: Circulation and transport dynamics in the Archipelago Sea, Ph.D. thesis, University of Helsinki, <http://hdl.handle.net/10138/587710>, 2024.
- 460 Mulsow, S., Boudreau, B. P., and Smith, J. A.: Bioturbation and porosity gradients, *Limnology and Oceanography*, 43, 1–9, 1998.
- Pascolo, S., Petti, M., and Bosa, S.: On the Wave Bottom Shear Stress in Shallow Depths: The Role of Wave Period and Bed Roughness, *Water*, 10, 1348, <https://doi.org/10.3390/w10101348>, 2018.
- Pettersson, H., Kahma, K. K., and Tuomi, L.: Wave Directions in a Narrow Bay, *Journal of Physical Oceanography*, 40, 155–169, <https://doi.org/10.1175/2009JPO4220.1>, 2010.
- 465 Roberts, J., Jepsen, R., Gotthard, D., and Lick, W.: Effects of Particle Size and Bulk Density on Erosion of Quartz Particles, *Journal of Hydraulic Engineering*, 124, 1261–1267, [https://doi.org/10.1061/\(ASCE\)0733-9429\(1998\)124:12\(1261\)](https://doi.org/10.1061/(ASCE)0733-9429(1998)124:12(1261)), 1998.
- Savela, M.: Hydrological and Sediment Dataset from the Tvärminne Coastal Area (2014–2015), Dataset, <https://doi.org/10.5281/zenodo.15796802>, 2025.

- 470 Schünemann, M. and Kühl, H.: A device for erosion measurements on naturally formed, muddy sediments: the EROMES-System, Tech. rep., GKSS Research Centre, 1991.
- Shields, A.: Anwendung der Ähnlichkeitsmechanik und der Turbulenzforschung auf die Geschiebebewegung, Preußische Versuchsanstalt für Wasserbau, Berlin, Germany, english translation available at: <http://authors.library.caltech.edu/25992/1/Sheilds.pdf>, 1936.
- Soulsby, R.: Dynamics of Marine Sands, Thomas Telford Publishing, London, UK, 1997.
- 475 Soulsby, R. L. and Whitehouse, R. J. S.: Threshold of Sediment Motion in Coastal Environments, Conference paper, <https://doi.org/10.3316/informit.929741720399033>, 1997.
- The SWAN team: SWAN scientific and technical documentation, Tech. rep., Delft University of Technology, <http://swanmodel.sourceforge.net/download/zip/swantech.pdf>, downloaded on 06.01.2026, 2024.
- Thompson, C. E. L., Williams, M. E., Amoudry, L., Hull, T., Reynolds, S., Pantong, A., and Fones, G. R.: Benthic controls of resuspension in
- 480 UK shelf seas: Implications for resuspension frequency, *Continental Shelf Research*, 185, 3–15, <https://doi.org/10.1016/j.csr.2017.12.005>, 2019.
- Valanko, S.: Dispersal and metacommunity dynamics in a soft-sediment benthic system: how well is the seafloor connected?, 2012.
- Westerlund, A., Tuomi, L., Alenius, P., Miettunen, E., and Vankevich, R. E.: Attributing mean circulation patterns to physical phenomena in the Gulf of Finland, *Oceanologia*, 60, 16–31, <https://doi.org/10.1016/j.oceano.2017.05.003>, 2018.
- 485 Zhang, G., Hu, S., Yu, X., Zhang, H., and Gong, W.: Physical drivers and parameter sensitivities of pearl river-derived sediment dispersal on the Northern South China Sea Shelf: a modeling study, *Ocean Science*, 21, 2041–2068, <https://doi.org/10.5194/os-21-2041-2025>, 2025.